nature sustainability

ARTICLES

https://doi.org/10.1038/s41893-022-00947-z

Check for updates

Sea-level rise from land subsidence in major coastal cities

Cheryl Tay[1,2]✉, Eric O. Lindsey[2,3], Shi Tong Chin[2], Jamie W. McCaughey[4], David Bekaert[5], Michele Nguyen[1], Hook Hua[5], Gerald Manipon[5], Mohammed Karim[5], Benjamin P. Horton[1,2], Tanghua Li[2] and Emma M. Hill[1,2]

Coastal land can be lost at rapid rates due to relative sea-level rise (RSLR) resulting from local land subsidence. However, the comparative severity of local land subsidence is unknown due to high spatial variabilities and difficulties reconciling observations across localities. Here we provide self-consistent, high spatial resolution relative local land subsidence (RLLS) velocities derived from Interferometric Synthetic Aperture Radar for the 48 largest coastal cities, which represent 20% of the global urban population. We show that cities experiencing the fastest RLLS are concentrated in Asia. RLLS is also more variable across the 48 cities (−16.2 to 1.1 mm per year) than the Intergovernmental Panel on Climate Change estimations of vertical land motion (−5.2 to 4.9 mm per year). With our standardized method, the identification of relative vulnerabilities to RLLS and comparisons of RSLR effects accounting for RLLS are now possible across cities worldwide. These will better inform sustainable urban planning and future adaptation strategies in coastal cities.

Sea-level rise resulting from climate change has rightly received substantial attention from researchers, practitioners and the public as an ongoing threat that needs to be addressed[1]. International efforts have thus been gathered through the Intergovernmental Panel on Climate Change (IPCC) to assess future risks of climate change and sea-level rise, and aid policymakers in developing sustainable adaptation and mitigation strategies[1]. Yet lesser attention has been paid to local land subsidence, which is the sinking of the ground at rates that can exceed tens of millimetres per year[2–4], and which can increase local relative sea-level rise (RSLR) many times that of global mean sea-level rise of a few millimetres per year alone[5,6]. Local RSLR, defined as sea-level rise relative to local land height, is what effectively matters for any coastal community. Furthermore, many of the coastal areas experiencing the fastest rates of local land subsidence are major cities built on flat, low-elevation river deltas, exposing large populations and substantial economic value to the impacts of local RSLR[7,8]. Consequently, it is crucial to consider local land subsidence when assessing future risks of RSLR for the sustainable development of coastal areas[9,10].

Local land subsidence is caused by groundwater, oil and gas extraction[2,4], and compaction of sediments occurring naturally due to self-weight[7,8]. It contributes to vertical land motion (VLM), but differs from other components of VLM such as regional tectonics[11,12] and glacial isostatic adjustment[13,14]. Because these components of VLM vary substantially over a range of temporal and spatial scales, the full contribution of VLM to RSLR has been difficult to assess comparatively between localities across the globe without restrictions to any region or location[15]. Many studies have mapped VLM at different coastal localities over different time spans[2–4,16–18] using Global Navigation Satellite System (GNSS)[16–19], tide gauges[17,19] (indirectly, as these measure relative sea level), geological observations[20] and interferometric synthetic aperture radar (InSAR)[2–4,17,18]. While point measurements such as those gained from GNSS, tide gauges and geological observations capture broader spatial patterns of VLM well, they do not capture the full range of localized spatial patterns of land subsidence[5,6]. For InSAR, the loss of coherence over vegetated areas, high computational costs and disparities in processing approaches, datasets and time spans are barriers to consolidating local land subsidence data from numerous existing studies[6]. Lacking consistent analyses of local land subsidence, RSLR assessments that compare cities and regions across the globe have either assumed VLM to be similar across localities based on their common characteristics[8,10,21], assumed VLM to be spatially uniform across each locality[7,22] or analysed VLM with point measurements[1,19,23]. Local land subsidence likely remains largely underestimated in these RSLR assessments, including in the IPCC Sixth Assessment Report (AR6)[1], with limited consideration of its magnitude and spatial variation[15,24].

We aim to contribute to future RSLR assessments by providing self-consistent observations of relative local land subsidence (RLLS) for the 48 largest coastal cities worldwide, which account for 20% of the global urban population[25]. We focus on InSAR, which given its continuous spatial extent and high resolution can fill gaps between point measurements from GNSS and tide gauges[5,6,17]. We employ best practices in a standardized InSAR processing approach to produce self-consistent observations and use cloud computing to address expensive computational requirements. The observations presented here allow for the identification of specific areas and neighbourhoods in cities that are undergoing rapid subsidence and thus facing accelerated RSLR and greater exposure to coastal hazards. The results also serve as a basis for future estimations of RSLR impacts that include the influence of RLLS consistently across coastal cities worldwide.

Variability of RLLS across cities

We derive velocities of RLLS by analysing Sentinel-1 InSAR data from 2014 to 2020 in 48 coastal cities and projecting line-of-sight

[1]Asian School of the Environment, Nanyang Technological University, Singapore, Singapore. [2]Earth Observatory of Singapore, Nanyang Technological University, Singapore, Singapore. [3]University of New Mexico, Albuquerque, NM, USA. [4]Institute for Environmental Decisions, Department of Environmental Systems Science, ETH Zürich, Zürich, Switzerland. [5]NASA Jet Propulsion Laboratory/Caltech, Pasadena, CA, USA. ✉e-mail: tayw0049@e.ntu.edu.sg

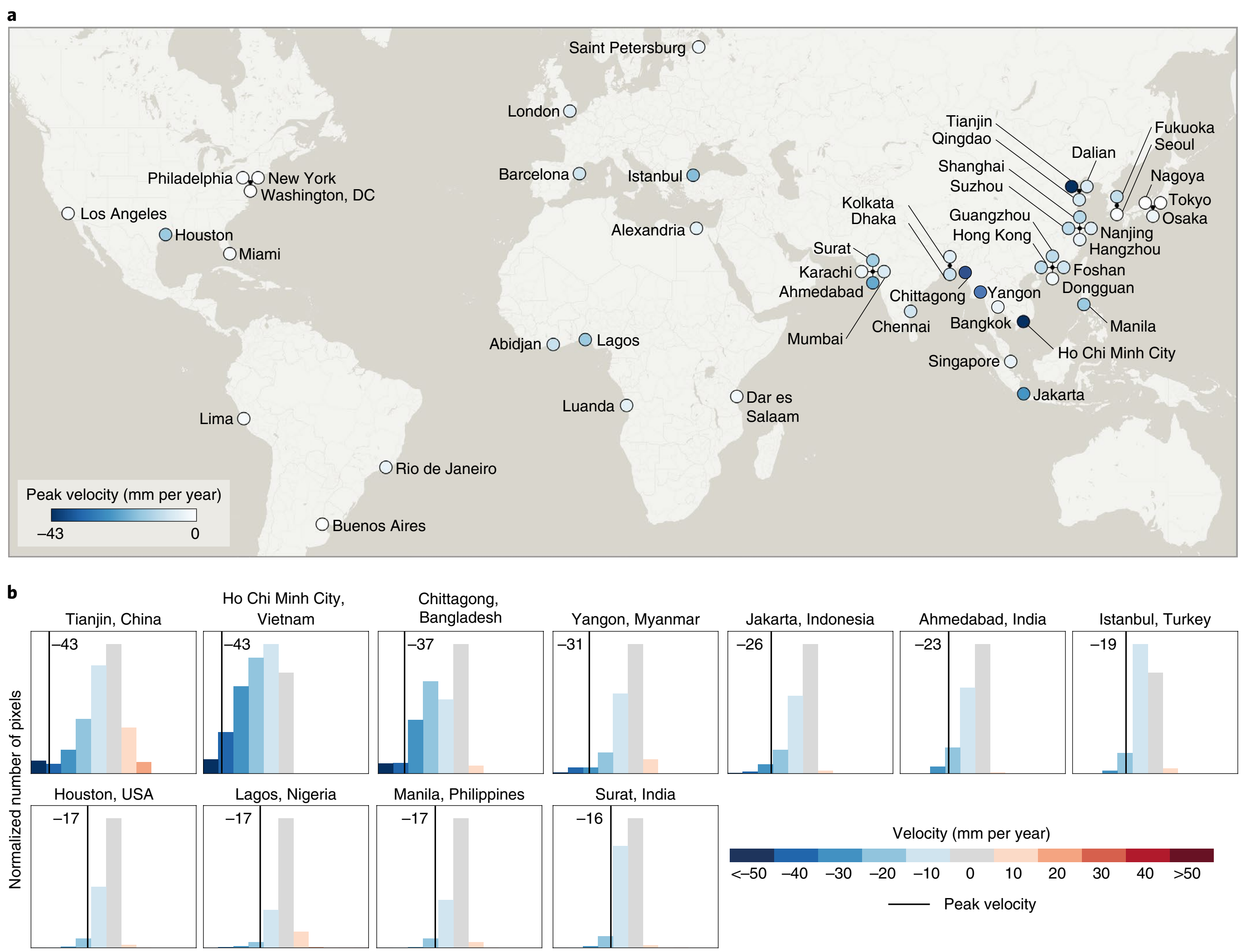

Fig. 1 | Peak RLLS velocities across the 48 coastal cities. a, The fastest peak RLLS velocities are concentrated in Asia. Peak velocity refers to the 95th percentile of negative InSAR velocities within the administrative boundary of a coastal city. Basemap data from Carto. **b**, Histograms of the normalized number of pixels associated with each range of InSAR velocities within the administrative boundaries of cities show that higher peak velocities coincide with higher proportions of subsiding areas. Peak velocities are indicated by black lines and upper-left numbers. Only cities with the highest peak velocities are shown; see Supplementary Section A for histograms of other cities.

velocities to the vertical with respect to the ground (Methods). Negative velocity refers to land subsidence or rise in mean sea level throughout this study. The velocities for each coastal city are relative to a nearby reference point within the synthetic aperture radar (SAR) images used, and linear trends spanning the SAR images are removed (Methods). The velocities therefore do not include broad-scale components of VLM such as due to regional tectonics[11,12] and glacial isostatic adjustment[13,14], although we assess the possible impact of these effects on VLM below.

First, a comparison across coastal cities worldwide shows that the fastest velocities of RLLS are concentrated in Asia, especially in Southeast Asia. We identify the 95th percentile of negative velocities as representative of the peak RLLS experienced by each coastal city (Fig. 1). Coastal cities experiencing notable RLLS with a 95th percentile velocity faster than −20 mm per year include Tianjin (China), Ho Chi Minh City (Vietnam), Chittagong (Bangladesh), Yangon (Myanmar), Jakarta (Indonesia) and Ahmedabad (India). Many of these fast-subsiding coastal cities are rapidly expanding megacities, where anthropogenic factors, such as high demands for groundwater extraction and loading from densely constructed building structures, contribute to local land subsidence[2,7,8,21].

It should be noted that the presented extreme velocities in these six coastal cities may be affected by the projection of InSAR line-of-sight velocities to the vertical[26] (Methods). The 95th percentile velocity also coincides with the overall prevalence of RLLS within each coastal city. For example, the six coastal cities with the highest 95th percentile velocities also have the largest proportion of subsiding areas (Fig. 1b). In the mid-range of the 95th percentile velocities, 21 of the 48 coastal cities have velocities faster than −10 mm per year (Fig. 1a). This is a rate well beyond both the millimetre precision of InSAR[27] and the typical standard deviations of our derived velocities (Figs. 3b and 4b). Next, 44 of the 48 coastal cities have 95th percentile velocities faster than the current global mean sea-level rise of −3.7 mm per year observed between 2006 and 2018 (ref. [1]) (Fig. 1a). These coastal cities are thus probably exposed to a greater extent of RSLR impacts due to the added contribution of RLLS if there is no substantial uplift contributed by other components of VLM. At the lower end of the spectrum, the remaining 4 of the 48 coastal cities are at relatively lower risk of increased RSLR impacts due to RLLS at current rates. These coastal cities include Seoul (South Korea), Tokyo (Japan), Washington DC (United States) and Nagoya (Japan) (Fig. 1a).

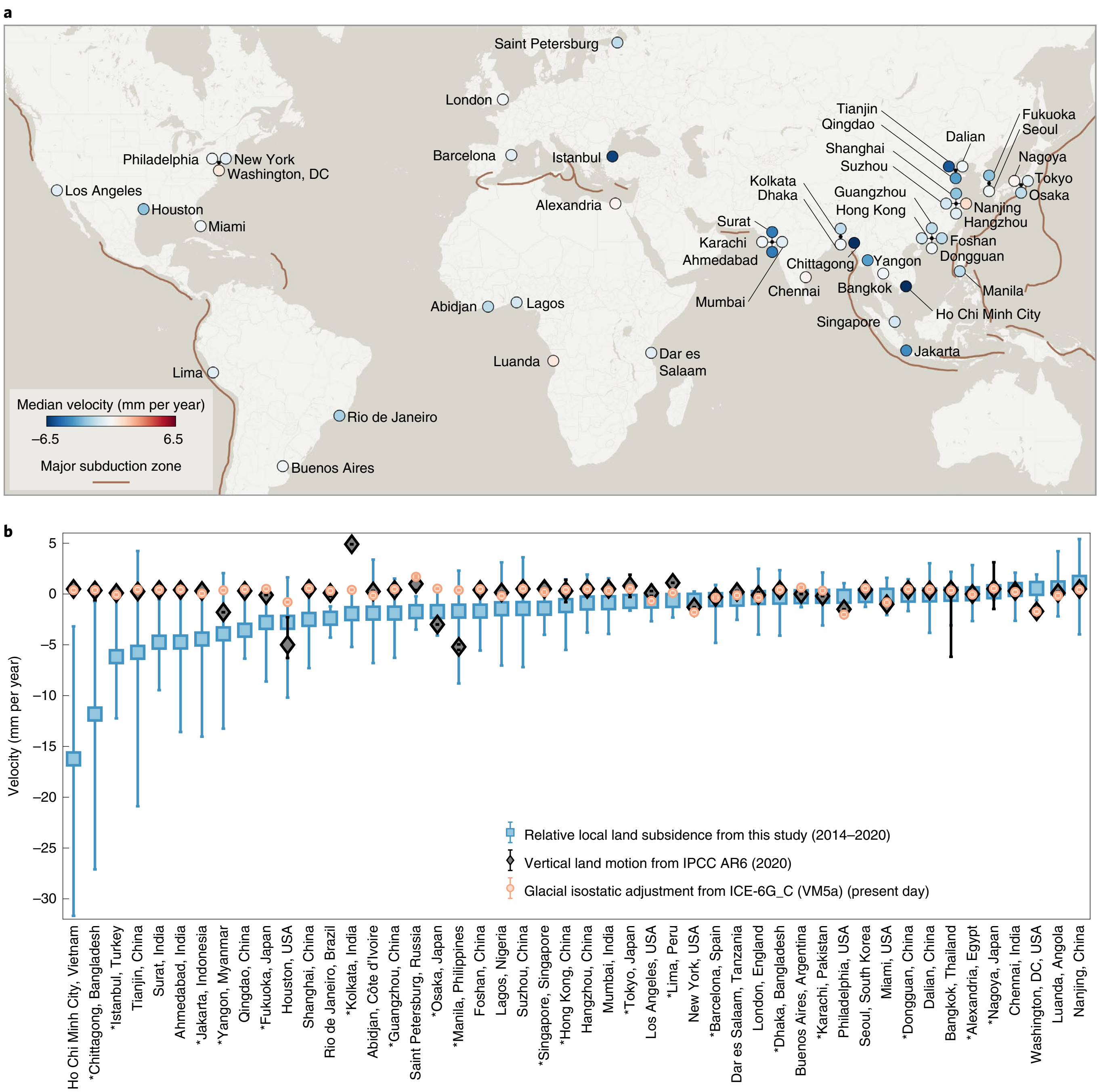

Fig. 2 | The range of RLLS across the 48 coastal cities. This range is wider than that of present-day glacial isostatic adjustment contributions to vertical land motion[29,30] and overall vertical land motion[1,28]. **a**, Median of RLLS velocities within each city. The same values are plotted in **b**. Basemap data from Carto. **b**, 16th, 50th (median) and 84th percentiles of different components of vertical land motion within each city. Wider ranges between the 16th and 84th percentiles indicate stronger spatial variability of velocities within a city itself. Note that the median velocities of RLLS may occur in areas at some elevation from mean sea level and comparison of the full map of velocities against topography would be needed for detailed consideration of relative sea-level changes. Asterisks indicate cities that are within 800 km of major subduction zones, obtained from the United States Geological Survey and plotted in **a**.

Next, RLLS contributions alone are more variable across coastal cities than IPCC AR6 estimates of present-day VLM. It should be noted that local land subsidence, tectonics and glacial isostatic adjustment are all major contributors of present-day VLM. We show the 16th, 50th (median) and 84th percentiles of all RLLS velocities within each coastal city in Fig. 2. The median RLLS of each coastal city ranges from −16.2 mm per year (Ho Chi Minh City, Vietnam) to 1.1 mm per year (Nanjing, China) across the 48 cities (Fig. 2). In comparison, the median VLM of each coastal city estimated in 2020 by the IPCC AR6 is more similar across the 48 cities and ranges from −5.2 to 4.9 mm per year (Fig. 2b)[1,28]. We suggest that the difference in the ranges is because local land subsidence contributions to VLM can be much larger than broad-scale contributors of VLM (tectonics and glacial isostatic adjustment), the latter of which being what the IPCC AR6 mainly captures. The IPCC AR6 rates were extrapolated from a quasi-global network of

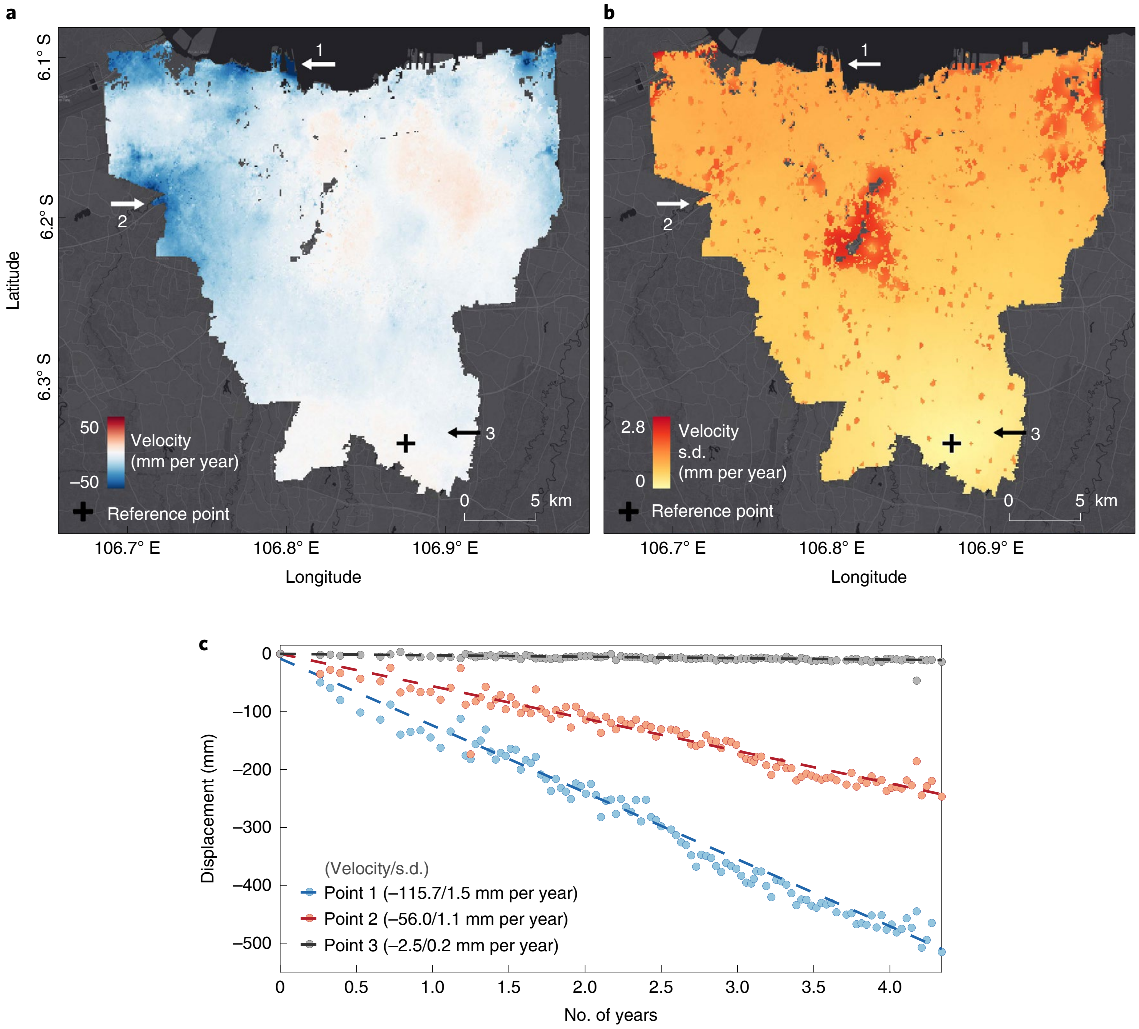

Fig. 3 | InSAR-derived velocities of RLLS in a coastal city with fast-subsiding areas, Jakarta (Indonesia). Subsiding clusters are concentrated in the urban areas of Penjaringan (point 1) and Kembangan District (point 2). **a**, RLLS velocities. **b**, Corresponding standard deviations (s.d.s) of velocities in **a**, which reflect the uncertainty and potential short-term non-linearity of velocities. **c**, Time series displacements at points 1, 2 and 3, where velocities with a better linear fit to the displacements have a lower standard deviation. Basemap data from ESRI.

point measurements recorded by tide gauges along coastlines[1]. The IPCC AR6 rates therefore reflect broad-scale VLM well, but do not reflect the full range of local land subsidence. This is as opposed to our analysis, at higher resolution and farther inland, to map local land subsidence, where coastal areas can still be impacted by RSLR. Amongst broad-scale contributors of VLM, earthquakes generating large tectonic VLM also likely affect only coastal cities near major subduction zones (Fig. 2) and occur as one-off, transient events. The range of median glacial isostatic adjustment across coastal cities considered in this study is small, ranging from −2.0 mm per year to 1.7 mm per year based on the basis of the widely used ICE-6G_C (VM5a) model[29,30] (Fig. 2b). We thus suggest, based on the range of RLLS velocities, that VLM may be more spatially variable across the world than currently assessed in the IPCC AR6. Observations beyond coastlines, such as those presented here, can then improve future assessments of VLM effects on RSLR.

Variability of RLLS within cities

Our results show high spatial variability of RLLS within each coastal city, underscoring the importance of measuring subsidence at high spatial resolution. The spatial distribution of RLLS is unique from city to city (Figs. 3 and 4, and Supplementary Section B). In coastal cities experiencing fast RLLS in many areas, such as Jakarta (Indonesia) (Fig. 3), using an average velocity or the fastest known velocity uniformly over the coastal city would likely overestimate subsidence in many areas and divert attention away from the most rapidly subsiding areas. This is because the subsiding areas are commonly localized in clusters, such as in the Penjaringan and Kembangan Districts in the case of Jakarta (Fig. 3a,c). While we do not investigate the cause of the clusters in this study, other site-specific studies[4,18,31] have found that local land subsidence varies based on the spatial distribution of both human activity, related to industrial, agricultural or aquacultural zones with rapid groundwater use, and subsurface geology, as some layers compact more easily than others. In coastal cities known to experience less extreme RLLS, such as New York (United States) (Fig. 4), mapping of spatial variation is beneficial because areas of more rapid subsidence may potentially be identified. It may also be misleading if point measurements of velocities were coincidentally only available at any small clusters of RLLS and extrapolated spatially. For example, in New York, the InSAR-derived results suggest that possible subsidence is only localized in the west of Breezy Point and should not be extrapolated eastward along the coast (Fig. 4a,c). We present the mapped RLLS velocities for the rest of the coastal cities in Supplementary Section B.

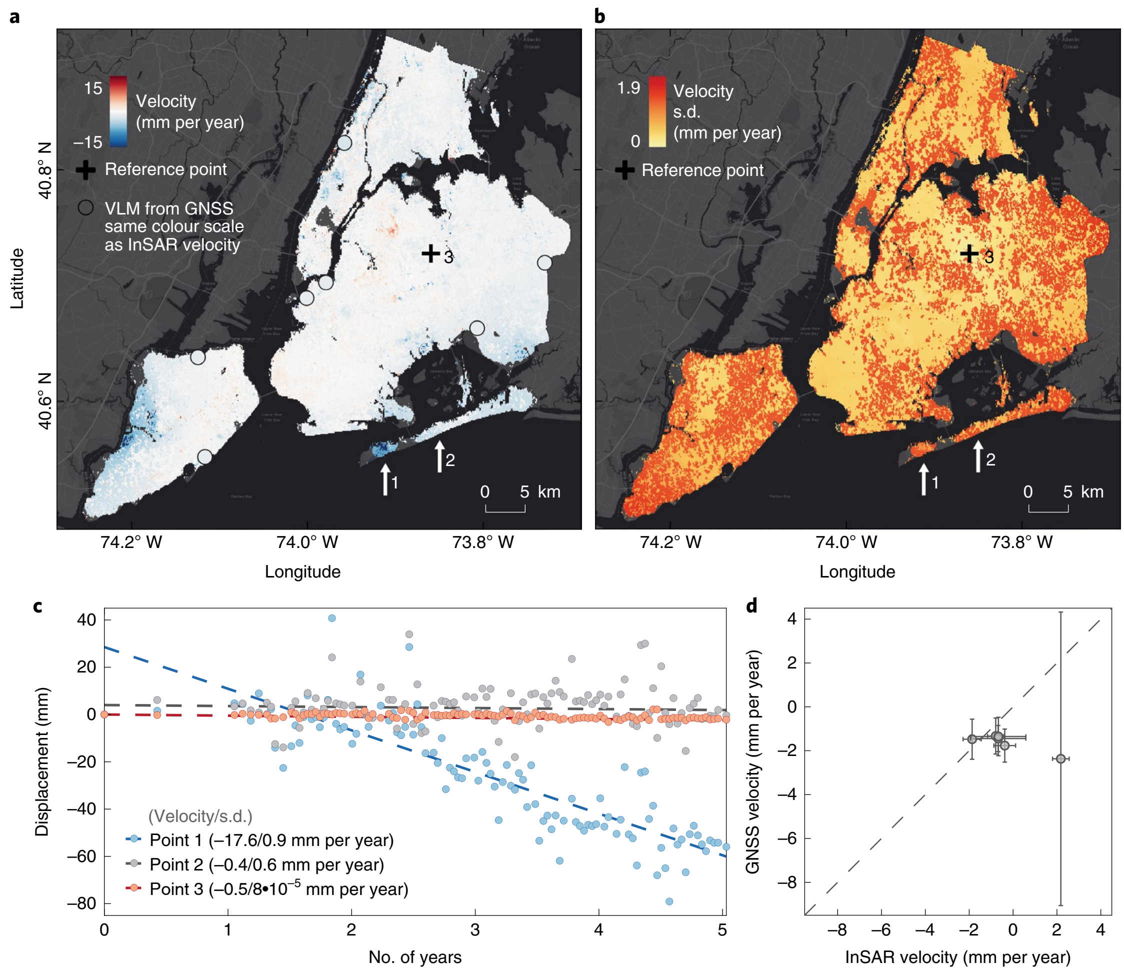

Fig. 4 | InSAR-derived velocities of RLLS in a coastal city with minimal subsidence, New York (USA). Subsidence is limited to locations such as at a small area of Breezy Point (point 1). **a**, RLLS velocities and point measurements of vertical land motion from Shirzaei et al.[6] using the same colour scale. **b**, Corresponding standard deviations of velocities in **a**, which reflect the uncertainty and potential short-term non-linearity of velocities. **c**, Time series displacements at points 1, 2 and 3, where velocities with a better linear fit to the displacements have a lower standard deviation. **d**, Comparison of InSAR and GNSS velocities and standard deviations at overlapping points shown in **a**. Note that direct comparisons of InSAR and GNSS should be avoided as the two instruments are sensitive to different types of land motion. Basemap data from ESRI.

Potential applications of RLLS

The observations we present may be used to estimate short-term RSLR impacts, which include the influence of RLLS. For example, a bathtub model comprising information on topography, mean sea-level rise and different components of VLM, including RLLS, could be used to compute the extent of inundation of a coastal city over the next decade. Topography from publicly accessible digital elevation models (DEMs) such as the Shuttle Radar Topography Mission (SRTM) may be several decades old, and VLM including contributions from RLLS can also be used to update the elevations to present-day levels. Since the local land subsidence velocities are relative, such applications for topography and bathtub analyses are most appropriate in coastal cities where information on the regional VLM is known and used to adjust relative values to the absolute in a stable reference frame. Regional VLM information could be from dense GNSS networks or known contributions of both glacial isostatic adjustment and regional tectonics. To illustrate the adjustment of the relative velocities, we provide two examples of bathtub analyses in Ho Chi Minh City (Vietnam) and Rio de Janeiro (Brazil), detailed in Supplementary Section C. The former coastal city has faster peak (Fig. 1) and median (Fig. 2) subsidence than the latter. We use steady-state local land subsidence projected over the next 10 years, up to 2030, in these examples (Supplementary Section C). The bathtub analyses show that the added effect of local land subsidence alone increases inundation extents by 20 km^2 and 2 km^2 in Ho Chi Minh City (Vietnam) and Rio de Janeiro (Brazil), respectively (Supplementary Section C).

Additionally, the RLLS velocities are a linear average of displacements from 2014 to 2020 and reflect steady-state velocities. Short-term non-linearity of the velocities can be accounted for using the corresponding standard deviations of velocities we provide. The standard deviations are computed from the goodness of fit between the linear velocity and displacements. These standard deviations therefore reflect uncertainties that could be associated with random error and short-term non-linearity, if present (Figs. 3b,c and 4b,c). However, the velocities may be accelerated, decelerated or even ceased in the long-term due to natural limiting factors such as the depletion or salinization of aquifers, or due to societal action such as changing the levels of natural resource extraction and introducing measures to stabilize coastal land[32,33]. These site-specific factors should be accounted for in analyses that examine how RLLS may influence long-term RSLR.

Discussion

We present a large-scale analysis of RLLS for the 48 most populous coastal cities worldwide, processed in a self-consistent manner and at high spatial resolution. These high spatial resolution results are complementary to, and greatly expand on, existing studies based on point measurements[1,19,23]. Our results are more representative of the spatial complexities of coastal subsidence that can occur at a local scale, but are intrinsically relative measurements that do not record absolute, total VLM. The RLLS velocities we provide also extend inland, where they are not measurable by tide gauges but where RSLR can still impact land and populations through flooding, storm surges and other extreme weather events. We suggest, based on the RLLS contributions, that VLM contributions to RSLR are likely more spatially variable across coastal cities than currently estimated in the IPCC AR6. This puts cities experiencing rapid local land subsidence at greater risk of coastal hazards than already present due to climate-driven sea-level rise. The large spatial variation and magnitude of RLLS exceeding tens of millimetres per year, compared to the smaller rates of climate-driven mean sea-level rise and glacial isostatic adjustment of a few millimetres per year, also show how RLLS could contribute to RSLR at a level on par, or potentially greater than other components of RSLR in many coastal cities. We thus highlight the importance of integrating these subsidence observations in future RSLR assessments to better inform sustainable planning.

We also present a standardized method of mapping RLLS that is readily extendable beyond the 48 coastal cities analysed. Potential future refinements of our RLLS velocities include: (1) extension of the analysis to metropolitan areas and neighbouring satellite cities, as these are future centres of population growth where subsidence may be aggravated by anthropogenic causes; and (2) continuation of the 6-year dataset to provide more robust statistics that account for longer-term non-linear trends in subsidence that may be unique to each coastal city.

This study provides a robust basis for estimating how local-scale land subsidence can compound the effects of climate-driven mean sea-level rise and represents a step towards accurate assessment of its impact across coastal cities worldwide. Our results are best suited for identifying relative vulnerabilities to land subsidence within each coastal city and for comparing the average velocities or the size of subsiding areas between coastal cities. The spatial footprints and velocities that we provide can be used to refine existing assessments of RSLR, and the effects of RLLS can be readily accounted for in risk assessments, adaptation options, appraisal and, ultimately, societal decisions. Our results also highlight a major need and opportunity for mitigation of coastal subsidence at the local, municipal level. Accelerated coastal subsidence is frequently caused by over-extraction of groundwater or, in some areas, extraction of gas or oil. When provided with a high-resolution map of subsidence in their area, affected communities are empowered to identify the causes and take direct action to reduce their future coastal risk, irrespective of actions taken by the rest of the world to address climate change and climate-driven mean sea-level rise.

Methods

Coastal city selection. We select the 48 largest coastal cities worldwide based on a minimum population of 5 million in 2020 and a maximum distance of 50 km from the coast. To account for the complexities in urban growth and extent, we refer to population sizes of urban agglomerations from the World Urbanization Prospects 2018 (ref. [25]). We also only select coastal cities where their administrative boundary contains elevations within 5 m from the mean sea level based on CoastalDEM[34], as elevations above 5 m are unlikely affected by RSLR. Administrative boundaries are obtained from OpenStreetMap (https://www.openstreetmap.org/) and modified by subtracting permanent water bodies, which are estimated from the European Space Agency Climate Change Initiative Water Bodies dataset[35]. CoastalDEM is based on the globally available National Aeronautics and Space Administration's SRTM Global 1 arc second Version 3.0 DEM[36], but has corrections applied over vegetation and densely populated areas to follow the height of the bare ground instead of the height of objects such as tall buildings standing on bare ground. CoastalDEM is thus suited for relative sea-level applications. Kuala Lumpur (Malaysia), Pune (India) and Sao Paulo (Brazil) are within the list of most populous coastal cities but were excluded due to the absence of elevations within 5 m of the mean sea level. Future work extending this analysis to the surrounding metropolitan areas and satellite cities would be especially warranted where these include areas within 5 m of mean sea level. Shenzhen (China) is also within the list of most populous coastal cities but was excluded due to InSAR processing errors (InSAR time series processing).

InSAR time series processing. In InSAR, the radar phase—related to the distance between the SAR satellite's sensor and target on the ground—of two SAR images acquired at different times is differenced to form an interferogram. Thus, the interferogram contains information on the relative change in land motion along the satellite's line-of-sight over a specific period, assuming a repeat-pass orbit where the SAR satellite returns to the same position over time. A connected series of interferograms that shows the time series of land motion can then be used to estimate the ground surface velocity, which is the long-term rate of land motion along the radar's line-of-sight. In addition to land motion, the interferogram also contains contributions from the troposphere, ionosphere, topography error, orbital error, residuals and noise, and these may be minimized through processing to preserve only contributions mainly from land motion.

We first download and process Sentinel-1 SAR images from October 2014 to April 2020 from either the ascending or descending orbit to create interferograms. The track with better spatial and temporal coverage of the coastal city is used. We use Sentinel-1 SAR imagery from the European Space Agency's Copernicus Sentinel programme as it is freely available, provides global coverage and, since 2014, has a high revisit frequency of 6 or 12 days. The native pixel resolution is approximately 5 m by 20 m. Downloads and interferogram processing are completed using the Advanced Rapid Imaging and Analysis Singapore (ARIA-SG) system (https://earthobservatory.sg/research/centres-labs/eos-rs) for scalability and ease of automation. ARIA-SG is a cloud-based SAR processing system, originally cloned from the Jet Propulsion Laboratory and California Institute of Technology's ARIA system (https://aria.jpl.nasa.gov/) and now co-developed by the Earth Observatory of Singapore. The system uses routine algorithms from the open-source InSAR Scientific Computing Environment (ISCE) software[37] to process interferograms. Using ARIA-SG, we create standard displacement products, which are phase-unwrapped interferograms processed using range and azimuth looks of 19 and 7, a Goldstein filter strength of 0.5, the enhanced spectral diversity co-registration method[38] and unwrapping through the Statistical-cost, Network-flow Algorithm for Phase Unwrapping[39]. The resulting interferograms are geocoded relative to the National Aeronautics and Space Administration's SRTM Global 3 arc second Version 3.0 dataset[40] at 90 m pixel spacing. To form a continuous time series of interferograms, each SAR image was paired with two other SAR images with the closest acquisition dates. Through the ARIA-SG system, we ensure no spatial or temporal gaps in each time series of interferograms and the use of consistent Sentinel-1 Instrument Processing Facility versions.

Next, we use the ARIA-tools software[41] to stitch together spatially adjacent interferograms that share identical date pairings. This involves the correction for integer multiples of 2π phase jumps at the overlapping area between two interferograms and the removal of additional bias from slant range pixel offset correction introduced during the routine ISCE processing of each interferogram[41]. We also use the ARIA-tools software to prepare interferograms in a compatible format for time series analysis in the Miami INsar Time series software in PYthon (MintPy).

Thirdly, we use routine Small BAseline Subset algorithms in MintPy[42] to perform time series analysis for each coastal city. The analysis is done pixel by pixel. A weighted least squares inversion is used to determine the long-term linear rate of land motion (velocity) of a pixel, based on the time series of interferograms. The standard deviation associated with each pixel's velocity is computed and equal to the goodness of fit between the predicted velocity (the best-fit linear line) and the land motion observed at each time epoch of the time series[43]. If non-linearity is present in the velocities, this would be reflected by higher standard deviations. We find the following MintPy processing parameters applicable and use these for the time series analysis of all coastal cities:

(1) Phase unwrapping error correction using bridging and phase closure methods to correct for phase jumps[42]
(2) Tropospheric delay correction based on the European Centre for Medium-Range Weather Forecasts ReAnalysis (ERA-5) Global Atmospheric Model[44], using the Python-based Atmospheric Phase Screen package[45,46] to remove unwanted tropospheric signals in C-band Sentinel-1 SAR
(3) Linear phase deramping to remove planar trends in velocities based on reliable pixels
(4) Topographic residual correction to reduce errors stemming from the DEM during interferogram processing[47]
(5) User-defined reference point for each coastal city

We show the effects of the above processing parameters on the velocity in Supplementary Section D. Parameters (2) to (4) typically result in adjustments at the mm level or less, which is relatively much smaller compared to parameters (1) and (5). For parameter (1), interferograms covering Shenzhen (China) have imperfect corrections for the phase unwrapping error, and so the coastal city is excluded from our analysis. Related to parameter (2), atmospheric noise caused by tropospheric delays of the SAR signal may be reduced further with future extension of our 6-year dataset. For each coastal city, a zero-velocity reference point, parameter (5), must be defined because InSAR observations are relative to an arbitrary local spatial reference—all velocities in an image are relative to the assumed velocity at the reference point. Ideally, a reference point with a known velocity from GNSS can be chosen to ensure that all velocities are fixed in an accurate reference frame. Due to the lack of such information in a consistent manner for all cities within our dataset, we instead choose a zero-velocity reference point from candidate pixels of a preliminary MintPy time series analysis. Our candidate pixels are located over man-made structures identified from Google Earth satellite images, which are considered to be stable, have a coherence greater than 0.85 across all dates and have a velocity close to the mode of velocities within the coastal city's administrative boundary. This method assumes that there is no broad-scale land motion and that most places have zero velocity within an administrative boundary. After choosing a reference point from among these candidate pixels, we run a second MintPy time series analysis with all pixel velocities computed relative to this point.

For each coastal city, we clip the InSAR images to the administrative boundary, with permanent water bodies excluded (Coastal city selection) since land motion rates are not applicable over pixels of water bodies. Finally, we exclude decorrelated pixels that have a coherence less than 0.35 from the time series analysis, as the phase is likely too noisy to reliably measure land motion at these pixels.

Spatial interpolation of InSAR velocities. Although the InSAR velocities from our time series analysis have dense spatial coverage, there are some spatial gaps in the data in areas where the InSAR pixels have undergone phase decorrelation due to vegetation growth or extensive land disturbance between images. These areas are automatically masked in our InSAR analysis; hence, we spatially interpolate the velocities across these gaps to produce a continuous map, assuming that land motions between nearby pixels are spatially correlated with each other. Since the velocity at each pixel is associated with its own standard deviation by virtue of the time series estimation, we adopt an approach that accounts for non-uniform standard deviations[48]. Like kriging, this approach relies on multivariate normal distributions. Whereas kriging assumes that all pixels have the same standard deviation, this extension allows for varying uncertainties and treats the pixels with higher standard deviations with less weight during the prediction based on the variogram[48] (Supplementary Section E).

Before implementing this interpolation method, we use a variance quadtree algorithm[49] to obtain a subset of the spatially dense velocities over each study region (Supplementary Section E). This helps to avoid redundancy while preserving the spatial variability of the velocities[49]. To quantify the spatial correlation in the velocities, we fit a spherical variogram via maximum likelihood estimation to the velocities of pixels associated with standard deviations lower than the mode. We treat these velocities as the base dataset and calculate the additional uncertainties in the other velocities relative to the mode of standard deviation. Since the interpolation method accounts for both the uncertainty from the time series analysis and the estimated spatial variability in the velocities as quantified by the variogram, the estimates typically have higher standard deviations than those derived directly from the time series analysis (Supplementary Section E). To avoid high estimation uncertainties at large distances from the data, we perform the interpolation only for pixels that have at least 40 pixels present within an 11-pixel radial distance, equivalent to an ~1 km radius. The final distribution of pixels may hence not provide complete coverage of the administrative boundary of a coastal city, but areas left unmapped are dominantly over vegetation where populations do not reside. The subsidence velocities we provide are thus most readily comparable across cities for built-up urban areas as opposed to vegetated land.

Projection of line-of-sight InSAR velocities to the vertical. To better represent the RLLS component of VLM, we project the line-of-sight velocity, v_{LOS}, from a single look direction to vertical velocity with respect to the ground, v_{U}, following equation (1).

$$v_{\mathrm{U}} = \frac{v_{\mathrm{LOS}}}{\cos\theta} \tag{1}$$

Here θ refers to the radar's incidence angle, which ranges between 29° and 41° across each Sentinel-1 SAR image used. We assume in this projection that there are no substantial gradients in the horizontal land motion because these are detrended through linear phase deramping (InSAR time series processing). Any constant horizontal land motion across the image, for example, due to plate tectonics, is accounted for by the assumption of a zero-velocity reference point (InSAR time series processing). The error in this line-of-sight to vertical projection scales with the magnitude of horizontal land motion, if any. As we focus on RLLS typically caused by natural resource extraction of groundwater, oil and gas, and sediment compaction due to self-weight, we expect in most coastal cities that vertical land motion will be more dominant than the horizontal and projection errors to be minimal. This assumption is commonly made in VLM studies[22] but could break down in areas where there are extreme magnitudes of land subsidence or large earthquakes that also induce substantial gradients in horizontal land motion around the subsiding area. This would slightly shift the apparent location of the maximum subsiding point towards the satellite look direction but would affect the magnitude only slightly due to the ratio of horizontal to vertical motions induced by the subsidence and the relative sensitivity of InSAR to these components of motion. To further refine the VLM velocities, future work can be done to incorporate observations from both look directions[26,50] (Supplementary Section F).

Reference to vertical land motion rates. The median VLM rate of each coastal city plotted in Fig. 2b is downloaded from the IPCC AR6 projection dataset (https://podaac.jpl.nasa.gov/announcements/2021-08-09-Sea-level-projections-from-the-IPCC-6th-Assessment-Report). The dataset contains network Common Data Form files of projected rates of different RSLR components, at different percentile levels, under different shared socioeconomic pathway (SSP) scenarios, in different years and at irregular points that are mostly spaced 1° apart across the globe. The RSLR components include VLM rates, with no distinction between different VLM contributions and mean sea-level rates due to Antarctic and Greenland ice sheets, glaciers, land water storage and ocean dynamics. The VLM rates are also identical across SSP scenarios[1,28]. Within this dataset, we use VLM rates at the 50th percentile, under the medium confidence, SSP2-4.5 scenario, in 2020, at data points within the administrative boundary of each coastal city. We then take the median of all these data points within the city. If there are no data points within the city, we search for data points within a 1° radial distance of its administrative boundary. We obtain the uncertainty of the median VLM rate of each coastal city in Fig. 2b by computing the 16th and 84th percentiles across the data points within the city (Supplementary Section G). The uncertainty in Fig. 2b thus reflects how strongly the data points may deviate from the median VLM rate in a city.

Reference to glacial isostatic adjustment rates. The median glacial isostatic adjustment rate of each coastal city plotted in Fig. 2b is downloaded from the published vertical rates of radial displacement dataset of the widely used ICE-6G_C (VM5a) model[29,30] (https://www.atmosp.physics.utoronto.ca/~peltier/data.php). The vertical rates of radial displacement refer to the VLM contribution due to glacial isostatic adjustment. The development of the ICE-6G_C (VM5a) model was constrained by observational data (for example, relative sea-level histories, GNSS, ice margin positions) from North America, Northern Europe, Barbados and Antarctica. Note that the model's performance in Asia needs improvement[51] as very limited observational data from Asia were used to constrain the model[30]. The rates are provided at gridded points spaced 0.2° apart across the globe. We only use rates at data points within the administrative boundary of each coastal city. We then take the median of all these data points within the city. We obtain the uncertainty of the median glacial isostatic adjustment rate of each coastal city in Fig. 2b by computing the 16th and 84th percentiles across the data points within the city (Supplementary Section G). The uncertainty is, overall, small compared to that of other components of VLM in Fig. 2b because glacial isostatic adjustment is a regional process that is relatively uniform over entire cities considered in this study.

Reporting summary. Further information on research design is available in the Nature Research Reporting Summary linked to this article.

Data availability

All replication data of RLLS velocities in this study are available in the following DR-NTU Data repository: https://doi.org/10.21979/N9/GPVX0F. The vertical land motion rates from the IPCC AR6 are publicly available at https://podaac-tools.jpl.nasa.gov/drive/files/misc/web/misc/IPCC/IPCC_AR6_slp_regional.tar.gz. Glacial isostatic adjustment rates from ICE-6G_C (VM5a) is publicly available at https://www.atmosp.physics.utoronto.ca/~peltier/data.php. Plate tectonic boundaries plotted in Fig. 2 are downloadable from https://www.usgs.gov/media/files/plate-boundaries-kmz-file. GNSS velocities plotted in Fig. 4 are downloadable from https://data.lib.vt.edu/articles/dataset/World_s_Coast_Vertical_Land_Motion/17710973. Source data are provided with this paper.

Code availability

All codes for the analysis of the datasets are available in the following DR-NTU Data repository: https://doi.org/10.21979/N9/GPVX0F. ARIA-SG algorithms, which contain ISCE algorithms, are accessible at: https://github.com/earthobservatory. Other InSAR processing algorithms including ARIA-Tools v1.1.1 and MintPy v1.3.0 are open-source and freely available through Github.

Received: 20 September 2021; Accepted: 21 July 2022;
Published online: 12 September 2022

References

1. IPPC *Climate Change 2021: The Physical Science Basis* (eds Masson-Delmotte, V. et al.) (Cambridge Univ. Press, 2021).
2. Chaussard, E., Amelung, F., Abidin, H. & Hong, S.-H. Sinking cities in Indonesia: ALOS PALSAR detects rapid subsidence due to groundwater and gas extraction. *Remote Sens. Environ.* **128**, 150–161 (2013).

3. Raucoules, D. et al. High nonlinear urban ground motion in Manila (Philippines) from 1993 to 2010 observed by DInSAR: implications for sea-level measurement. *Remote Sens. Environ.* **139**, 386–397 (2013).
4. Aobpaet, A., Cuenca, M. C., Hooper, A. & Trisirisatayawong, I. InSAR time-series analysis of land subsidence in Bangkok, Thailand. *Int. J. Remote Sens.* **34**, 2969–2982 (2013).
5. Higgins, S. A. Advances in delta-subsidence research using satellite methods. *Hydrol. J.* **24**, 587–600 (2016).
6. Shirzaei, M. et al. Measuring, modelling and projecting coastal land subsidence. *Nat. Rev. Earth Environ.* **2**, 40–58 (2021).
7. Ericson, J. P., Vörösmarty, C. J., Dingman, S. L., Ward, L. G. & Meybeck, M. Effective sea-level rise and deltas: causes of change and human dimension implications. *Glob. Planet. Change* **50**, 63–82 (2006).
8. Syvitski, J. P. et al. Sinking deltas due to human activities. *Nat. Geosci.* **2**, 681–686 (2009).
9. Dasgupta, S., Laplante, B., Murray, S. & Wheeler, D. *Sea-level Rise and Storm Surges: A Comparative Analysis of Impacts in Developing Countries* World Bank Policy Research Working Paper (World Bank, 2009).
10. Hanson, S. et al. A global ranking of port cities with high exposure to climate extremes. *Clim. Change* **104**, 89–111 (2011).
11. Wiseman, K., Bürgmann, R., Freed, A. M. & Banerjee, P. Viscoelastic relaxation in a heterogeneous Earth following the 2004 Sumatra–Andaman earthquake. *Earth Planet. Sci. Lett.* **431**, 308–317 (2015).
12. Qiu, Q., Moore, J. D., Barbot, S., Feng, L. & Hill, E. M. Transient rheology of the Sumatran mantle wedge revealed by a decade of great earthquakes. *Nat. Commun.* **9**, 995 (2018).
13. Love, R. et al. The contribution of glacial isostatic adjustment to projections of sea-level change along the Atlantic and Gulf coasts of North America. *Earth's Future* **4**, 440–464 (2016).
14. Ding, K., Freymueller, J. T., He, P., Wang, Q. & Xu, C. Glacial isostatic adjustment, intraplate strain, and relative sea level changes in the eastern United States. *J. Geophys. Res.: Solid Earth* **124**, 6056–6071 (2019).
15. Wöppelmann, G. & Marcos, M. Vertical land motion as a key to understanding sea level change and variability. *Rev. Geophys.* **54**, 64–92 (2016).
16. Zhao, R. et al. Rapid land subsidence in Tianjin, China derived from continuous GPS observations (2010–2019). *Proc. Int. Assoc. Hydrological Sci.* **382**, 241–247 (2020).
17. Brooks, B. et al. Space geodetic determination of spatial variability in relative sea level change, Los Angeles basin. *Geophys. Res. Lett.* **34**, L01611 (2007).
18. Abidin, H. Z. et al. in *IAG 150 Years: International Association of Geodesy Symposia* Vol. 143 (eds Rizos, C. & Willis, P.) 435–442 (Springer, 2015).
19. Pfeffer, J. & Allemand, P. The key role of vertical land motions in coastal sea level variations: a global synthesis of multisatellite altimetry, tide gauge data and GPS measurements. *Earth Planet. Sci. Lett.* **439**, 39–47 (2016).
20. Engelhart, S. E., Horton, B. P., Douglas, B. C., Peltier, W. R. & Törnqvist, T. E. Spatial variability of late Holocene and 20th century sea-level rise along the Atlantic coast of the United States. *Geology* **37**, 1115–1118 (2009).
21. Nicholls, R. J., Hoozemans, F. M. & Marchand, M. Increasing flood risk and wetland losses due to global sea-level rise: regional and global analyses. *Glob. Environ. Change* **9**, S69–S87 (1999).
22. Nicholls, R. J. et al. A global analysis of subsidence, relative sea-level change and coastal flood exposure. *Nat. Clim. Change* **11**, 338–342 (2021).
23. Ostanciaux, E., Husson, L., Choblet, G., Robin, C. & Pedoja, K. Present-day trends of vertical ground motion along the coast lines. *Earth Sci. Rev.* **110**, 74–92 (2012).
24. Nicholls, R. J. & Cazenave, A. Sea-level rise and its impact on coastal zones. *Science* **328**, 1517–1520 (2010).
25. United Nations, Department of Economic and Social Affairs, Population Division. *World Urbanization Prospects: The 2018 Revision* (United Nations, 2019).
26. Fuhrmann, T. & Garthwaite, M. C. Resolving three-dimensional surface motion with InSAR: constraints from multi-geometry data fusion. *Remote Sens.* **11**, 241 (2019).
27. Rucci, A., Ferretti, A., Guarnieri, A. M. & Rocca, F. Sentinel 1 SAR interferometry applications: the outlook for sub millimeter measurements. *Remote Sens. Environ.* **120**, 156–163 (2012).
28. Garner, G. G. et al. IPCC AR6 Sea-Level Rise Projections v.20210809 (PO.DAAC, 2021).
29. Argus, D. F., Peltier, W., Drummond, R. & Moore, A. W. The Antarctica component of postglacial rebound model ICE-6G_C (VM5a) based on GPS positioning, exposure age dating of ice thicknesses, and relative sea level histories. *Geophys. J. Int.* **198**, 537–563 (2014).
30. Peltier, W. R., Argus, D. & Drummond, R. Space geodesy constrains ice age terminal deglaciation: the global ICE-6G_C (VM5a) model. *J. Geophys. Res.: Solid Earth* **120**, 450–487 (2015).
31. Erban, L. E., Gorelick, S. M. & Zebker, H. A. Groundwater extraction, land subsidence, and sea-level rise in the Mekong Delta, Vietnam. *Environ. Res. Lett.* **9**, 084010 (2014).
32. de Graaf, I. E., Gleeson, T., van Beek, L. R., Sutanudjaja, E. H. & Bierkens, M. F. Environmental flow limits to global groundwater pumping. *Nature* **574**, 90–94 (2019).
33. Minderhoud, P., Middelkoop, H., Erkens, G. & Stouthamer, E. Groundwater extraction may drown mega-delta: projections of extraction-induced subsidence and elevation of the Mekong delta for the 21st century. *Environ. Res. Commun.* **2**, 011005 (2020).
34. Kulp, S. A. & Strauss, B. H. CoastalDEM: a global coastal digital elevation model improved from SRTM using a neural network. *Remote Sens. Environ.* **206**, 231–239 (2018).
35. Lamarche, C. et al. Compilation and validation of SAR and optical data products for a complete and global map of inland/ocean water tailored to the climate modeling community. *Remote Sens.* **9**, 36 (2017).
36. NASA Shuttle Radar Topography Mission Global 1 arc second (NASA JPL, 2013); https://doi.org/10.5067/MEASURES/SRTM/SRTMGL1.003
37. Rosen, P. A., Gurrola, E., Sacco, G. F. & Zebker, H. The InSAR scientific computing environment. In *EUSAR 2012; 9th European Conference on Synthetic Aperture Radar* (Eds. Guarnieri, A. M. & Scheiber, R.) 730–733 (VDE, 2012).
38. Bekaert, D. et al. Development of open-access Standardized InSAR Displacement Products by the Advanced Rapid Imaging and Analysis (ARIA) Project for Natural Hazards. In *AGU Fall Meeting Abstracts* G23A-04 (AGU, 2019).
39. Chen, C. W. & Zebker, H. A. Network approaches to two-dimensional phase unwrapping: intractability and two new algorithms. *J. Opt. Soc. Am. A* **17**, 401–414 (2000).
40. NASA Shuttle Radar Topography Mission Global 3 arc second (NASA JPL, 2013); https://doi.org/10.5067/MEASURES/SRTM/SRTMGL3.003
41. Buzzanga, B., Bekaert, D. P., Hamlington, B. D. & Sangha, S. S. Toward sustained monitoring of subsidence at the coast using InSAR and GPS: an application in Hampton Roads, Virginia. *Geophys. Res. Lett.* **47**, e2020GL090013 (2020).
42. Yunjun, Z., Fattahi, H. & Amelung, F. Small baseline InSAR time series analysis: unwrapping error correction and noise reduction. *Comput. Geosci.* **133**, 104331 (2019).
43. Fattahi, H. & Amelung, F. InSAR bias and uncertainty due to the systematic and stochastic tropospheric delay. *J. Geophys. Res.: Solid Earth* **120**, 8758–8773 (2015).
44. Dee, D. P. et al. The ERA-Interim reanalysis: configuration and performance of the data assimilation system. *Q. J. R. Meteorol. Soc.* **137**, 553–597 (2011).
45. Jolivet, R., Grandin, R., Lasserre, C., Doin, M. & Peltzer, G. Systematic InSAR tropospheric phase delay corrections from global meteorological reanalysis data. *Geophys. Res. Lett.* **38**, L17311 (2011).
46. Jolivet, R. et al. Improving InSAR geodesy using global atmospheric models. *J. Geophys. Res.: Solid Earth* **119**, 2324–2341 (2014).
47. Fattahi, H. & Amelung, F. DEM error correction in InSAR time series. *IEEE Trans. Geosci. Remote Sens.* **51**, 4249–4259 (2013).
48. Worden, C. B. et al. Spatial and spectral interpolation of ground-motion intensity measure observations. *Bull. Seismol. Soc. Am.* **108**, 866–875 (2018).
49. Bagnardi, M. & Hooper, A. Inversion of surface deformation data for rapid estimates of source parameters and uncertainties: a Bayesian approach. *Geochem. Geophys. Geosyst.* **19**, 2194–2211 (2018).
50. Wright, T. J., Parsons, B. E. & Lu, Z. Toward mapping surface deformation in three dimensions using InSAR. *Geophys. Res. Lett.* **31**, L01607 (2004).
51. Chua, S. et al. A new Holocene sea-level record for Singapore. *Holocene* **31**, 1376–1390 (2021).

Acknowledgements

We thank the European Union Copernicus and European Space Agency for acquiring Sentinel-1 data, and Amazon Web Services for their provision of the Public Dataset Program to enable the download of Sentinel-1 data in the Asia region (https://registry.opendata.aws/sentinel1-slc-seasia-pds/). This research is supported by the Earth Observatory of Singapore (EOS), the National Research Foundation (NRF), Singapore, and the Ministry of Education (MOE), Singapore, under the Research Centres of Excellence initiative, by a Singapore NRF Investigatorship (Award ID NRF-NRFI05-2019-0009) and a Singapore MOE Tier 3 grant (Award ID MOE2019-T3-1-004) awarded to E.M.H. This research is also supported by the NRF, Singapore, and National Environment Agency, Singapore, under the National Sea Level Programme Initiative as part of the Urban Solutions & Sustainability – Integration Fund (Award No. USS-IF-2020-5) by a grant (Award ID NSLP-2021-3R-05) awarded to E.M.H. The research was carried out, in part, at the Jet Propulsion Laboratory, California Institute of Technology, under a contract with the National Aeronautics and Space Administration. T.L. and B.P.H. are supported by the Singapore MOE Academic Research Fund (MOE-T2EP50120-0007). This work comprises EOS contribution number 445.

Author contributions

C.T., E.O.L., E.M.H. and J.W.M. were responsible for the conceptualization of the work. C.T., E.O.L., D.B. and M.N. were responsible for the methodology. Data processing

was carried out by C.T. and S.T.C. S.T.C., C.T., D.B., H.H., G.M., M.K. and M.N. were responsible for the software. C.T., E.O.L., D.B., M.N., B.P.H., T.L. and E.M.H. undertook the formal analysis and investigation. C.T. prepared the original draft. E.O.L, E.M.H., J.W.M, M.N., D.B., B.P.H, T.L. and S.T.C reviewed and edited the manuscript. E.M.H. and D.B. were responsible for funding acquisition.

Competing interests
The authors declare no competing interests.

Additional information
Supplementary information The online version contains supplementary material available at https://doi.org/10.1038/s41893-022-00947-z.

Correspondence and requests for materials should be addressed to Cheryl Tay.

Peer review information *Nature Sustainability* thanks Gonéri le Cozannet, Julia Pfeffer and Shimon Wdowinski for their contribution to the peer review of this work.

nature research

Corresponding author(s): Cheryl Tay
Last updated by author(s): Jun 18, 2022

Reporting Summary

Nature Research wishes to improve the reproducibility of the work that we publish. This form provides structure for consistency and transparency in reporting. For further information on Nature Research policies, see our Editorial Policies and the Editorial Policy Checklist.

Statistics

For all statistical analyses, confirm that the following items are present in the figure legend, table legend, main text, or Methods section.

n/a	Confirmed	
☐	☒	The exact sample size (n) for each experimental group/condition, given as a discrete number and unit of measurement
☒	☐	A statement on whether measurements were taken from distinct samples or whether the same sample was measured repeatedly
☒	☐	The statistical test(s) used AND whether they are one- or two-sided *Only common tests should be described solely by name; describe more complex techniques in the Methods section.*
☒	☐	A description of all covariates tested
☒	☐	A description of any assumptions or corrections, such as tests of normality and adjustment for multiple comparisons
☐	☒	A full description of the statistical parameters including central tendency (e.g. means) or other basic estimates (e.g. regression coefficient) AND variation (e.g. standard deviation) or associated estimates of uncertainty (e.g. confidence intervals)
☒	☐	For null hypothesis testing, the test statistic (e.g. F, t, r) with confidence intervals, effect sizes, degrees of freedom and P value noted *Give P values as exact values whenever suitable.*
☒	☐	For Bayesian analysis, information on the choice of priors and Markov chain Monte Carlo settings
☒	☐	For hierarchical and complex designs, identification of the appropriate level for tests and full reporting of outcomes
☒	☐	Estimates of effect sizes (e.g. Cohen's d, Pearson's r), indicating how they were calculated

Our web collection on statistics for biologists contains articles on many of the points above.

Software and code

Policy information about availability of computer code

Data collection	ARIA-SG algorithms used to download data are accessible at: https://github.com/earthobservatory.
Data analysis	All codes for the analysis of the datasets are available in the following DR-NTU Data repository: https://doi.org/10.21979/N9/GPVX0F. ARIA-SG algorithms which contain ISCE algorithms are accessible at: https://github.com/earthobservatory. Other InSAR processing algorithms including ARIA-Tools v1.1.1 and MintPy v1.3.0 are open-source and freely available through Github.

For manuscripts utilizing custom algorithms or software that are central to the research but not yet described in published literature, software must be made available to editors and reviewers. We strongly encourage code deposition in a community repository (e.g. GitHub). See the Nature Research guidelines for submitting code & software for further information.

Data

Policy information about availability of data

All manuscripts must include a data availability statement. This statement should provide the following information, where applicable:

- Accession codes, unique identifiers, or web links for publicly available datasets
- A list of figures that have associated raw data
- A description of any restrictions on data availability

All replication data of relative local land subsidence velocities in this study are available in the following DR-NTU Data repository: https://doi.org/10.21979/N9/GPVX0F. The vertical land motion rates from the IPCC AR6 are publicly available at https://podaac-tools.jpl.nasa.gov/drive/files/misc/web/misc/IPCC/IPCC_AR6_slp_regional.tar.gz. Glacial isostatic adjustment rates from ICE-6G_C (VM5a) is publicly available at https://www.atmosp.physics.utoronto.ca/~peltier/data.php. Plate tectonic boundaries plotted in Fig. 2 are downloadable from https://www.usgs.gov/media/files/plate-boundaries-kmz-file. GNSS velocities plotted in Fig. 4 are downloadable from https://data.lib.vt.edu/articles/dataset/World_s_Coast_Vertical_Land_Motion/17710973.

Field-specific reporting

Please select the one below that is the best fit for your research. If you are not sure, read the appropriate sections before making your selection.

☐ Life sciences ☐ Behavioural & social sciences ☒ Ecological, evolutionary & environmental sciences

For a reference copy of the document with all sections, see nature.com/documents/nr-reporting-summary-flat.pdf

Ecological, evolutionary & environmental sciences study design

All studies must disclose on these points even when the disclosure is negative.

Study description	For each coastal city we selected, we downloaded and processed Synthetic Aperture Radar (SAR) data to extract velocities of relative local land subsidence. We computed and presented the 95th percentile of negative velocities and the 16th, 50th (median), and 84th percentiles of velocities for each city. We also compared the median and spread of the relative local land subsidence velocities against that of published rates of other components of vertical land motion. Lastly, we used the relative local land subsidence velocities in bathtub models to estimate land areas that will be below mean sea-level in 2030 for two selected coastal cities. We used the mean and +/- one standard deviation of the velocities to compute upper and lower bounds to show the uncertainties associated with the mean estimate.
Research sample	We analyzed SAR data acquired over 48 coastal cities. The SAR data acquired by Copernicus Sentinel-1 satellites operated by the European Space Agency are freely accessible through the Copernicus Open Access Hub. We also referred to existing data of these cities that were published by others. These existing data include vertical land motion rates from the Intergovernmental Panel on Climate Change Sixth Assessment Report (IPCC AR6) and glacial isostatic adjustment rates from the ICE-6G_c (VM5a) model which are both freely accessible.
Sampling strategy	The 48 most populous coastal cities worldwide were selected for analysis, as these are where majority of relative sea-level rise impacts are felt by people. We selected the 48 coastal cities based on a minimum population of 5 million in 2020 and a maximum distance of 50 km from the coast. We also only select coastal cities that are more likely affected by RSLR, if its administrative boundary contains elevations within 5 m from the mean sea-level. We referred to population sizes from the World Urbanization Prospects 2018 dataset and elevations from CoastalDEM, both of which are freely accessible.
Data collection	The SAR data were acquired by the European Space Agency. We downloaded the SAR data from their open access site using ARIA-SG algorithms (https://github.com/earthobservatory).
Timing and spatial scale	For each coastal city, we downloaded all SAR data captured over the city from a single satellite track that were acquired by the Copernicus Sentinel-1 satellite between October 2014 and April 2020. The track with the best spatial and temporal coverage of the coastal city was selected.
Data exclusions	All SAR scenes must have the same Sentinel-1 Instrument Processing Facility (IPF) versions to be processed together, hence SAR scenes with incompatible IPF versions were excluded. Kuala Lumpur (Malaysia), Pune (India), and Sao Paulo (Brazil) are within the list of most populous coastal cities but excluded due to the absence of elevations within 5 m from the mean sea-level. Shenzhen (China) is also within the list of most populous coastal cities but excluded due to InSAR processing errors (see "InSAR time series processing").
Reproducibility	The ARIA-SG algorithms (https://github.com/earthobservatory) used to download SAR data, filter out SAR scenes with incompatible IPF versions, and process the data, and ARIA-Tools (https://github.com/aria-tools/ARIA-tools) and MintPy (https://github.com/insarlab/MintPy/tree/main/mintpy) algorithms used to process the data, are all archived in Github. Code used to load all information of the IPCC AR6 vertical land motion rates and ICE-6G_c (VM5a) glacial isostatic adjustment rates are made available (https://doi.org/10.21979/N9/GPVX0F). Repeated use of all algorithms give the same result as no randomization is involved. Parameters used for each algorithm are documented in the main text.
Randomization	The processing of relative local land subsidence velocities and calculations of land area and population below mean sea-level involve no randomization. No experiments were conducted.
Blinding	This study is based on remote sensing data i.e. SAR data acquired by satellites. No experiments or surveys were conducted.

Did the study involve field work? ☐ Yes ☒ No

Reporting for specific materials, systems and methods

We require information from authors about some types of materials, experimental systems and methods used in many studies. Here, indicate whether each material, system or method listed is relevant to your study. If you are not sure if a list item applies to your research, read the appropriate section before selecting a response.

Materials & experimental systems

n/a	Involved in the study
☒	☐ Antibodies
☒	☐ Eukaryotic cell lines
☒	☐ Palaeontology and archaeology
☒	☐ Animals and other organisms
☒	☐ Human research participants
☒	☐ Clinical data
☒	☐ Dual use research of concern

Methods

n/a	Involved in the study
☒	☐ ChIP-seq
☒	☐ Flow cytometry
☒	☐ MRI-based neuroimaging